

Polarization Detection of Terahertz Waves using All-Silicon Metasurfaces with Tightly Focusing Behavior

Hui Li, Chenglong Zheng, Shouxin Duan, Jie Li, Hang Xu, Yifan Li, Chunyu Song, Fan Yang, Zhen Yue, Wei Shi, Yating Zhang,* Yun Shen,* and Jianquan Yao*

The manipulation of polarization states is reflected in the tailoring of light–matter interactions and has great applications in fundamental science. Nevertheless, the conventional polarization-separated detection behavior in the terahertz (THz) band is very challenging when applied to visualize the incident polarization state since its measurement requires sophisticated instrumentation. Here, the feasibility of its reconstruction of the full-Stokes parameter matrix in the THz band is explored by establishing an all-silicon decoupled metasurface based on the polarization multiplexing encoding technique. The pixelated focal spots gathered in the target plane allow us to employ more elaborate methods to extract the characteristic parameters of the incident polarization states. The resolvability of the THz polarization detection behavior with a single focal spot is further optimized benefiting from the longitudinal polarization component (E_z) generated by the tightly focused beam in the propagation direction. The capability of the E_z -component in determining the key parameters that compose the polarization ellipse is evaluated by predefining the random incident polarization on a standard Poincaré sphere. Thus, the proposed scheme offers significant advantages in future THz communications, providing opportunities for ultra-compact, high-resolution full-Stokes polarization imaging and multidimensional information processing.

for optics-related applications such as optical communications,^[1] navigation,^[2] and remote sensing.^[3] The full-Stokes parameter matrix is typically employed to evaluate the polarization state carried by the incident wave, which can be determined by measuring the intensity of the three pairs of orthogonal polarization components contained within the matrix.^[4,5] Stokes polarization detection technology is an emerging technology that can be used to detect and analyze the structure, material, composition, and surface state of objects. Conventional approaches for measuring the full-Stokes parameter matrix are typically divided into single- and multi-optical path measurements.^[6,7] However, to the best of our knowledge, traditional polarization measurement systems involve separated and bulky components to distinguish different incident polarization states, which leads to slow response and limited accuracy of the polarization system in collecting SoP. Moreover, applications requiring discrete components for alignment are difficult to combine the two functions

1. Introduction

State of polarization (SoP) is an inherent property of electromagnetic (EM) waves, detailing the oscillatory direction of the electric field along the propagation path, and homogenous profiles typically include linear, circular, and elliptical. Therefore, exploring techniques for characterizing polarization states is critical

of polarization detection and wavefront manipulation into one system.^[8,9] Therefore, it is very challenging to determine the SoP of THz waves during transmission quickly and with high accuracy.


In recent years, metasurfaces have offered a new opportunity for polarization-related applications due to their ultra-compact structural design.^[10–12] As nanostructures capable of obtaining

H. Li, C. Zheng, J. Li, H. Xu, C. Song, F. Yang, Z. Yue, W. Shi, Y. Zhang, J. Yao
Key Laboratory of Opto-Electronics Information Technology (Tianjin University)
Ministry of Education, School of Precision Instruments and Opto-Electronics Engineering, Tianjin University
No. 92 Weijin Road, Tianjin 300072, China
E-mail: yating@tju.edu.cn; jqyao@tju.edu.cn

S. Duan, Y. Shen
Department of Physics, School of Physics and Materials Science
Nanchang University
Nanchang 330031, China
E-mail: shenyun@ncu.edu.cn

J. Li
Information Materials and Device Applications Key Laboratory of Sichuan Provincial Universities
Chengdu University of Information Technology
Chengdu 610225, China

Y. Li
College of Electronic Information Engineering & Hebei Key Laboratory of Digital Medical Engineering
Hebei University
Baoding 071000, China

 The ORCID identification number(s) for the author(s) of this article can be found under <https://doi.org/10.1002/lpor.202300428>

DOI: 10.1002/lpor.202300428

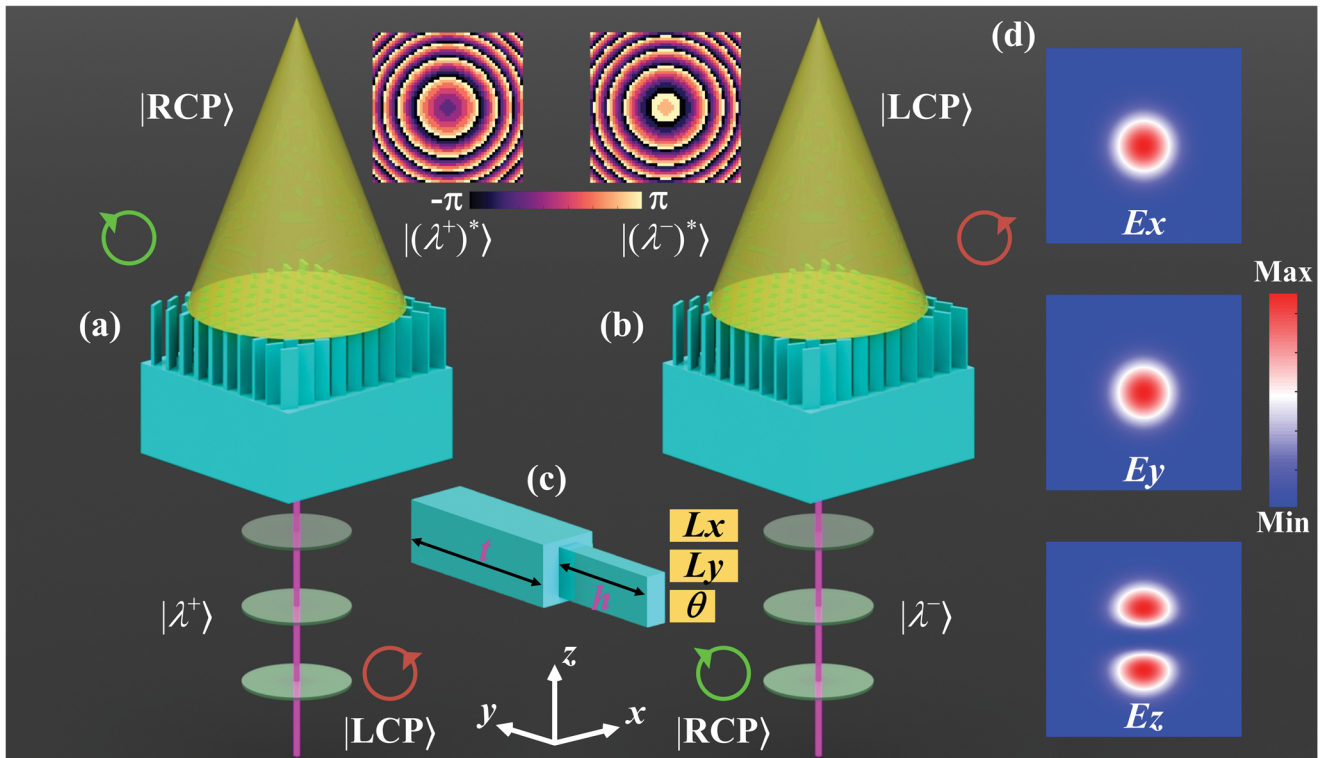


Figure 1. Working principle of the decoupled metasurface with central focusing characteristics. a) Schematic diagram of a meta-platform with a single focusing effect within an RCP channel under LCP illumination. b) Schematic diagram of a meta-platform with a single focusing effect within an LCP channel under RCP illumination. c) Geometric parameters of the designed meta-atoms with anisotropy. d) The focal spot produced under x-polarized illumination observed in a pre-designed focal plane, including the E_x , E_y , and E_z -components, can be utilized to reconstruct the basic information of the incident polarization state. The phase maps embedded in the LCP and RCP channels, respectively, are shown at the top of the figure.

full-Stokes parameters in a single snapshot, and artificially designed meta-atoms can be integrated directly with complementary metal oxide semiconductors (CMOS).^[13–17] Related applications that have been demonstrated include circular polarization detection,^[12–14] full polarization measurements,^[18–21] polarization imaging,^[22–24] and so on. Pors et al. successfully reconstructed the full-Stokes parameter matrix in the visible range using a reflective plasmonic meta-grating. The resolution of the polarization state for the incident light is determined by measuring the corresponding diffraction intensity.^[18] Arbabi et al. demonstrate a new design for full-Stokes polarization measurement based on all-dielectric metasurfaces at the working wavelength about 850 nm. Such metasurface can split and focus light in three different polarization bases with spatial separation properties.^[20] Sun et al. demonstrated the behavior of full-Stokes polarization spectral imaging with highly integrated properties in the wavelength range of 1400–1700 nm for spatially multiplexed all-dielectric metasurfaces. Three pairs of typical orthogonal polarization states can be reconstructed from the full-Stokes parameter matrix consisting of three sets of off-axis sub-metalens.^[25] However, to the best of our knowledge, the metasurface design regarding THz polarization detection with significant advantages in high-resolution imaging is more challenging due to the limitation of the emission efficiency of the integrated THz source. Although a reflective metasurface operating in the low THz band has been theoretically proposed for reconstructing the incident

polarization state, the array design with four focal points presents certain losses in experimental validation.^[26]

In this work, a minimalist method is demonstrated for reconstructing the full-Stokes parameter matrix and visualized polarization ellipse of incident THz waves based on the generation of polarization multiplexing tightly focused beams, as shown in **Figure 1a,b**. As a proof of concept, the proposed all-dielectric metasurface consists of an array of subwavelength-spaced rectangular silicon columns used as birefringent waveplates with a central operating frequency of 0.8 THz. The advanced Jones calculus imparts independent and arbitrary phase profiles to the two orthogonal circular polarization channels, allowing the proposed design to efficiently split the incident polarization states. The metasurface with spatial polarization separation based on the hexagonal lattice configuration has a relatively large error in determining the conventional incident polarization in the THz range. This is because the insertion loss of conventional THz waveplates is much higher than that of optical waveplates when measuring the full-Stokes parameters.^[27] Subsequently, we modified the conventional separated polarization detection for the superiority of the THz near-field scanning system, i.e., the full-Stokes parameters were reconstructed using multiplexed metasurfaces with single-point focusing characteristics. The pixelated focal spots assembled on the focal plane allow us to employ more elaborate algorithms to extract the key parameters of the incident random polarization state. To further emphasize

the resolvability of the multiplexed metasurface with single focusing capability, the incident THz waves are evaluated in detail using the longitudinal (axial) electric field component (E_z) carried by the tightly focused beams, as shown in Figure 1d. More interestingly, the encoding behavior for the orthogonal circularly polarized (CP) channel will induce spin-orbit coupling effects in the E_z -component. As far as we know, there are almost no reports on the visualization of incident polarization states in the THz band using the generated E_z -components. The experimental results demonstrated by such design schemes in polarization measurements are in good agreement with the simulated results. Thus, the demonstrated all-silicon metasurface offers a potential opportunity for efficient, high-resolution full-Stokes polarization devices operating in the THz band.

2. Design and Methods

The working mechanism of the THz polarization detection instrument with focused beams based on polarization multiplexing technique is illustrated in Figure 1. Benefiting from the subtle capabilities of the all-silicon multiplexed metasurface for wavefront manipulation, a simplified version of the full-Stokes meta-polarizer can be generated by imparting independent focused phase profiles within the orthogonal CP channels, as shown in Figure 1a,b. To obtain the phase distribution as shown in the inset in Figure 1, we applied the advanced Jones calculus to derive the required constraints. The Jones vector in the orthogonal CP channel for a meta-atom operating in a linear polarization basis can be expressed as follows^[28–30]

$$\begin{cases} |\lambda^+\rangle = \begin{bmatrix} \lambda_x^+ \\ \lambda_y^+ \end{bmatrix} = \begin{bmatrix} 1 \\ i \end{bmatrix} \\ |\lambda^-\rangle = \begin{bmatrix} \lambda_x^- \\ \lambda_y^- \end{bmatrix} = \begin{bmatrix} 1 \\ -i \end{bmatrix} \end{cases} \quad (1)$$

where “+” and “-” denote the handedness of circular polarization states, representing the left-handed circularly polarized (LCP) and right-handed circularly polarized (RCP) waves, respectively. The subscripts “x” and “y” indicate the coordinate components of the Cartesian coordinate system. The polarization state carried by the transmitted THz wave following the anisotropic design of the meta-atom supported by the spin decoupling principle is its complex conjugate with respect to each input circular polarization state, which can be expressed as $|\lambda^+\rangle \rightarrow |(\lambda^+)^*\rangle$ and $|\lambda^-\rangle \rightarrow |(\lambda^-)^*\rangle$, where * represents the complex conjugate. In order to impose the desired phase profiles into a pair of orthogonal CP channels, $\phi^+(x, y)$ and $\phi^-(x, y)$ with one-to-one correspondence are embedded in different channels with handedness $|\lambda^+\rangle$ and $|\lambda^-\rangle$, respectively. The independent manipulation of the LCP and RCP channels requires that the Jones matrix of each meta-atom in the generated metasurface satisfies the following relationship, i.e.

$$\begin{cases} J(x, y) \cdot |\lambda^+\rangle = e^{i\phi^+(x, y)} \cdot |(\lambda^+)^*\rangle \\ J(x, y) \cdot |\lambda^-\rangle = e^{i\phi^-(x, y)} \cdot |(\lambda^-)^*\rangle \end{cases} \quad (2)$$

For two orthogonal linear polarizations (e.g., x- and y-polarization, i.e., $0^\circ/90^\circ$), the Jones matrix $J(x, y)$ can be expressed as

$$J(x, y) = \begin{bmatrix} e^{i\phi^+(x, y)} & 0 \\ 0 & e^{i\phi^-(x, y)} \end{bmatrix} \quad (3)$$

Due to the diagonal symmetry of the target matrix $J(x, y)$, the geometrical parameters of the rectangular silicon column with birefringent properties can be directly modified to obtain a purely propagating phase modulation profile without the geometric phase modulation generated by the rotation of the silicon column. For a general polarimeter with polarization separation characteristics, using a simple coordinate transformation, the spatial spin-multiplexing of the 45° and 135° linearly polarized states can be achieved by rotating each rectangular silicon column in the previous configuration by 45° with respect to the x-direction, as shown in Figure S1 (Supporting Information Note S1). Subsequently, by mathematical transformation and derivation, the new Jones matrix can be used to characterize the orthogonal circular polarization incidence behavior, such as RCP and LCP, as follows

$$J(x, y) = \begin{bmatrix} e^{i\phi^+(x, y)} \cdot \begin{bmatrix} \lambda_x^+ \\ \lambda_y^+ \end{bmatrix} & e^{i\phi^-(x, y)} \cdot \begin{bmatrix} \lambda_x^- \\ \lambda_y^- \end{bmatrix} \\ e^{i\phi^+(x, y)} \cdot \begin{bmatrix} \lambda_x^+ \\ \lambda_y^+ \end{bmatrix} & e^{i\phi^-(x, y)} \cdot \begin{bmatrix} \lambda_x^- \\ \lambda_y^- \end{bmatrix} \end{bmatrix} \begin{bmatrix} |\lambda_x^+\rangle & |\lambda_x^-\rangle \\ |\lambda_y^+\rangle & |\lambda_y^-\rangle \end{bmatrix}^{-1} \quad (4)$$

Detailing the integration of the above-mentioned calculus, the Jones matrix of the multiplexed metasurface under orthogonal CP illumination can be described as

$$\begin{aligned} J(x, y) &= \begin{bmatrix} e^{i\phi^+(x, y)} & e^{i\phi^-(x, y)} \\ -i \cdot e^{i\phi^+(x, y)} & i \cdot e^{i\phi^-(x, y)} \end{bmatrix} \begin{bmatrix} 1 & 1 \\ i & -i \end{bmatrix}^{-1} \\ &= \frac{1}{2} \begin{bmatrix} e^{i\phi^+(x, y)} + e^{i\phi^-(x, y)} & -i \cdot e^{i\phi^+(x, y)} + i \cdot e^{i\phi^-(x, y)} \\ -i \cdot e^{i\phi^+(x, y)} + i \cdot e^{i\phi^-(x, y)} & -e^{i\phi^+(x, y)} - e^{i\phi^-(x, y)} \end{bmatrix} \end{aligned} \quad (5)$$

It is worth mentioning that the desired Jones matrix is unitary and symmetric, which means that the input and output THz waves have the same polarization ellipse, but an opposite handedness, so it can be recast as its canonical form

$$\begin{aligned} J(x, y) &= \begin{bmatrix} \cos \theta(x, y) & -\sin \theta(x, y) \\ \sin \theta(x, y) & \cos \theta(x, y) \end{bmatrix} \begin{bmatrix} e^{i\phi_x(x, y)} & 0 \\ 0 & e^{i\phi_y(x, y)} \end{bmatrix} \\ &\quad \begin{bmatrix} \cos \theta(x, y) & -\sin \theta(x, y) \\ \sin \theta(x, y) & \cos \theta(x, y) \end{bmatrix}^{-1} \end{aligned} \quad (6)$$

By ingeniously combining Equations (5) and (6) to be able to eliminate the unknown terms in the matrix, the correspondence of the desired key parameters for different polarization bases can be obtained as follows^[31–33]

$$\begin{cases} \phi_x(x, y) = \frac{1}{2} (\phi^+(x, y) + \phi^-(x, y)) \\ \phi_y(x, y) = \frac{1}{2} (\phi^+(x, y) + \phi^-(x, y)) - \pi \\ \theta(x, y) = \frac{1}{4} (\phi^+(x, y) - \phi^-(x, y)) \end{cases} \quad (7)$$

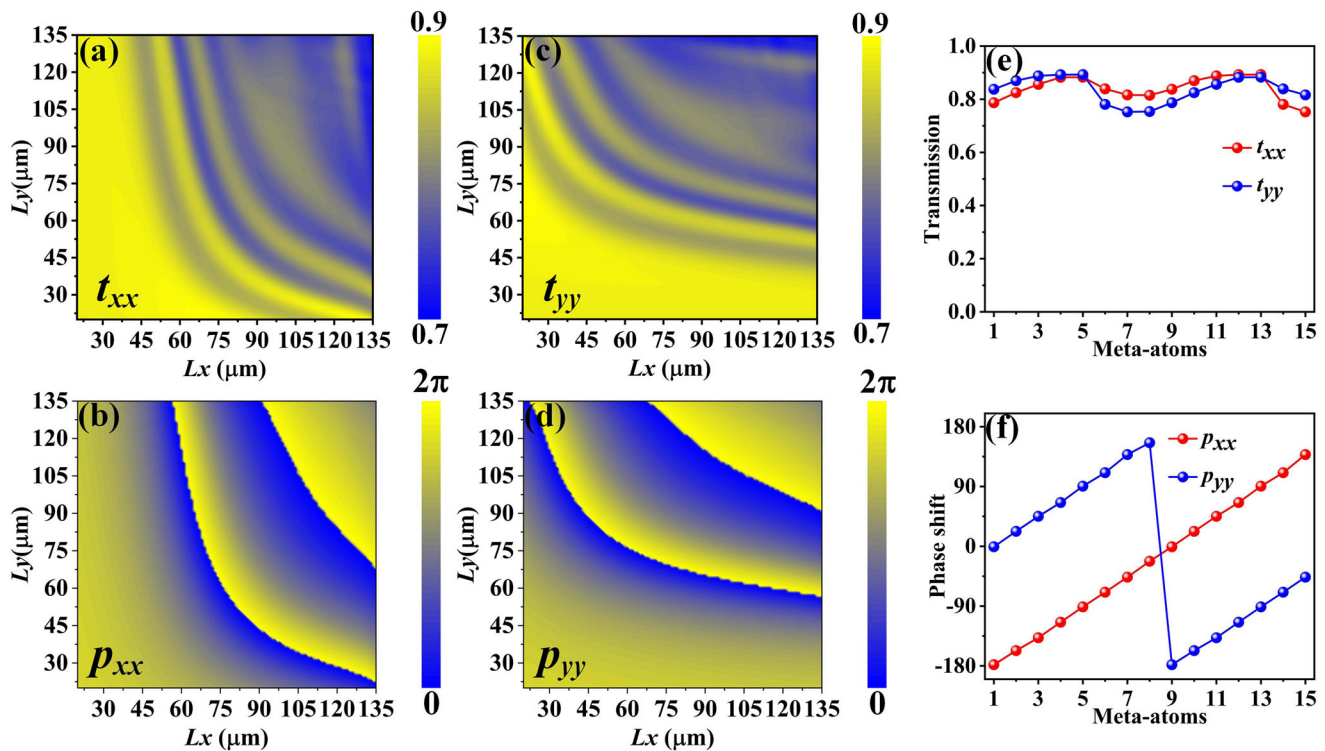


Figure 2. Amplitude and phase response of meta-atoms with periodic boundary conditions produced under linearly polarized illumination. a,b) The obtained transmission amplitudes and phase shifts of the meta-atoms with different geometric sizes under x-polarized incidence. c,d) The obtained transmission amplitudes and phase shifts of the meta-atoms with different geometric sizes under y-polarized incidence. The e) amplitudes and f) phase responses of the selected 15 meta-atoms that satisfy the constraints of Equation (7).

Compared to the meta-atoms in the diamond-shaped region for linearly polarized incidence, as mentioned in Figure S1 (Supporting Information Note S1), the selected elements that meet the decoupling condition have a phase interval of 22.5° in the limit of Equation (7). Furthermore, the operating behavior of the selected meta-atoms is characterized as rotatable half-wave retarders (HWRs), i.e., satisfying $|t_x(x, y)| = |t_y(x, y)|$ as well as $\varphi_x(x, y) + \pi = \varphi_y(x, y)$ under linearly polarized illumination. Also, an orientation angle $\theta(x, y)$ of the fast-axis as a function of the global coordinate systems. In other words, the decoupling operation for orthogonal circular polarization channels is achieved by a combination of propagation phase and geometric phase responses. The adopted meta-atoms with anisotropy exhibit a rectangular initial configuration and the key parameters determining their geometry are defined as L_x , L_y , and $\theta(x, y)$. In addition, the height of the silicon column is $h = 400 \mu\text{m}$ and the thickness of the substrate is $t = 600 \mu\text{m}$, as shown in Figure 1c. Subsequently, we monitored the normalized magnetic field intensity of the meta-atom at an operating frequency of 0.8 THz under x-polarized illumination, as shown in Figure S3 (Supporting Information Note S2). The presence of the Mie resonance allows the energy carried by the incident wave to be localized within the silicon column with a high refractive index ($\epsilon = 11.9$, and $\sigma = 0.00025 \text{ S m}^{-1}$ (Electric cond.)), implying that the interference coupling between two adjacent meta-atoms composing the metasurface can be neglected.^[34] The transmission coefficients as well as the phase retardations of the building blocks shown in Figure 2a–d were obtained by scanning a wide range of the key

parameters L_x and L_y that determine the geometric configuration of the meta-atoms under linearly polarized illumination. In fact, multiplexed beams are achieved by manipulating both the propagation phase and the geometric phase of the selected meta-atoms, which can impart a higher degree of freedom to the combined phase profile. Here, the propagation phase is defined in the Cartesian coordinate system as φ_x and φ_y , respectively, and is obtained by changing the dimensions of the anisotropic elements along the x- and y-directions. As shown in Figure 2e, the metasurface with all-silicon configuration exhibits high transmission amplitudes under x- and y-polarized illumination due to Fabry–Perot resonance, respectively, and the variation of t_{xx} and t_{yy} is limited to the range of 0.7–0.9. While the transmission phase under different polarization incidence has appreciable coverage from 0 to 2π , as shown in Figure 2f. The geometric phase employment process, however, is defined by the orientation angle $\theta(x, y)$ of the meta-atom, which can be obtained by rotating the meta-atom in the counterclockwise direction. The elaborated meta-array with individual focusing characteristics enables pixelated full-Stokes polarization measurement by selecting the 15 meta-atoms that satisfy the assembly requirements. Subsequently, the selected meta-atoms are expanded into an 8×8 matrix that satisfies a gradient arrangement with a phase interval of 22.5° under CP basis. The geometric parameters of the selected basic building blocks can be found in the Supporting Information Note S3. It is worth mentioning that the independent phase encoding profiles effectively simplify the arithmetic process of determining the classical full-Stokes parameter matrix.

3. Results and Discussions

Since the insertion loss present in the THz polarization measurement system is much higher than that in IR optics, the error in the THz range is relatively large by the conventional method of measuring Stokes parameters in a separated configuration. As shown in **Figure 3**, different from the polarization detection behavior with polarization separation characteristics that presents a rhombic lattice (Supporting Information Note S1), the proposed design principle distinguishes the key parameters that constitute the full-Stokes matrix by monitoring the different polarization components. As shown in **Figure 1**, the phase distribution embedded within the orthogonal CP channel will lead to a focal spot on the metasurface located at the center of the focal plane. It is important to emphasize that the measured focusing behavior of each polarization component at the focal plane contains a total of 800×800 pixel factors. To further visualize the trajectory of the electric field of the polarization state carried by the incident THz wave, the homogenous values of the complex amplitudes of the electric fields at the three-pixel points (400, 399), (400, 400), and (400, 401) are adopted to reconstruct the transmitted full-Stokes parameter matrix as well as the polarization ellipse. By pixelating the complex amplitude of the intensity distribution at the focal plane, the presented polarization ellipse can be described as^[34–36]

$$\begin{cases} \frac{E_x^2}{E_{0x}^2} + \frac{E_y^2}{E_{0y}^2} - 2 \frac{E_x E_y}{E_{0x} E_{0y}} \cos \delta = \sin^2 \delta \\ \delta = \delta_x - \delta_y \end{cases} \quad (8)$$

where E_x and E_y denote the monitored horizontal and vertical components of the total electric field, respectively. E_{0x} and E_{0y} represent the maximum amplitudes in the x - and y -directions, δ_x , and δ_y are the initial phase responses of the simulated E_x - and E_y -components, respectively. Subsequently, the incident and transmitted polarization ellipses were plotted by taking the complex amplitudes of the monitored electric fields at each central spot representing the different illumination modes. Obviously, the six polarization components can be visualized by recording the obtained polarization ellipse at each focal spot occupied pixel by Equation (8) and correspond one by one to the normalized Stokes matrix.

A scanning electron microscope image of this meta-platform with nonpolarization separation properties, fabricated using standard UV lithography and inductively coupled plasma (ICP) deep silicon etching techniques,^[37–39] is shown in **Figure 3a,b**. It is not surprising that the rectangular outlines of the blocks contained in the meta-arrays are well defined and the sidewalls are quite steep. For more detailed information on the sample preparation, see the Experimental Section. As proof-of-concept experiments, the predefined electric field intensity profile in the $z = 5$ mm plane was characterized using a fiber-based THz near-field detecting system,^[31,40] as shown in **Figure 3c**. The detailed measuring steps can be found in the Experimental Section too.

Monochromatically polarized plane waves propagating along the z -direction carrying arbitrary polarization modes can be ex-

pressed in terms of the Jones vector when located in the Cartesian coordinate system as follows^[41–43]

$$\mathbf{E} = \begin{pmatrix} \tilde{E}_x \\ \tilde{E}_y \end{pmatrix} = \begin{pmatrix} A_x e^{i\delta_1} \\ A_y e^{i\delta_2} \end{pmatrix} \quad (9)$$

here $\tilde{E}_x = E_x^{\text{Re}} + iE_x^{\text{Im}}$, $\tilde{E}_y = E_y^{\text{Re}} + iE_y^{\text{Im}}$, respectively, denote the complex amplitudes of the different polarization components at the central pixel spot, where E_i^{Re} and E_i^{Im} ($i = x, y$) are the real and imaginary parts of the electric field distribution on the focal plane. A_x and A_y indicate the magnitude projection along the horizontal and vertical linearly polarization axis, δ_1 and δ_2 represent the phase shift of A_x and A_y components. According to the established functional relationship between the six polarization components of the full-Stokes parameter matrix, it is known that $E_{45^\circ} = (\tilde{E}_x + \tilde{E}_y)/\sqrt{2}$, $E_{135^\circ} = (\tilde{E}_x - \tilde{E}_y)/\sqrt{2}$, $E_R = (\tilde{E}_x + i\tilde{E}_y)/\sqrt{2}$, and $E_L = (\tilde{E}_x - i\tilde{E}_y)/\sqrt{2}$. To characterize the polarization response of the meta-device, we first illuminate it with six basis polarization states ($0^\circ/90^\circ$, $45^\circ/135^\circ$, and LCP/RCP) in successive order. Subsequently, we obtained the measurement results for different polarization component at the focal plane separately using the standard algorithm. The function employed to reconstruct the full-Stokes parameter matrix $\mathbf{S} = [S_0, S_1, S_2, S_3]^T$ at the target pixel spots is modified to that^[20,44]

$$S_0 = A_x^2 + A_y^2 \quad (10a)$$

$$S_1 = A_x^2 - A_y^2 \quad (10b)$$

$$S_2 = 2A_x A_y \cos(\delta_1 - \delta_2) = A_{45^\circ}^2 - A_{135^\circ}^2 \quad (10c)$$

$$S_3 = 2A_x A_y \sin(\delta_1 - \delta_2) = A_R^2 - A_L^2 \quad (10d)$$

where A_{45° and A_{135° represent the amplitude projection along linearly diagonal and antidiagonal polarized, and A_R , A_L indicate the amplitude projection over RCP and LCP states. As can be seen in **Figure 3d**, the parameter matrix calculated by combining the E_x - and E_y -components indicates that the measurement results are in good agreement with the simulation results. It is worth noting that each of the remaining polarization components, i.e., E_{45° , E_{135° , E_R , and E_L have equal normalized intensities when the polarization mode carried by the incident wave is fixed to x -polarization, as mentioned in the Supporting Information Note S2. Therefore, the obtained histograms from the full-Stokes parameters are dominated by S_1 only, but S_2 and S_3 are absent. In addition, the polarization ellipse drawn by taking the complex amplitude at the central pixel point strongly illustrates the effectiveness of the design approach for reproducing the profile of the incident polarization. Similarly, the Stokes parameter matrix reconstructed from the multiplexed metasurface with a single focused spot under y -polarized illumination proves the consistency of the experimental results, as shown in **Figure 3e**. On the other hand, the selected meta-atoms from the established database are constructed as the HWR ($\Delta = \pi$). Thus, the encoding behavior based on the pair of orthogonal CP channels determines that the proposed design exhibits significant flipping characteristics in

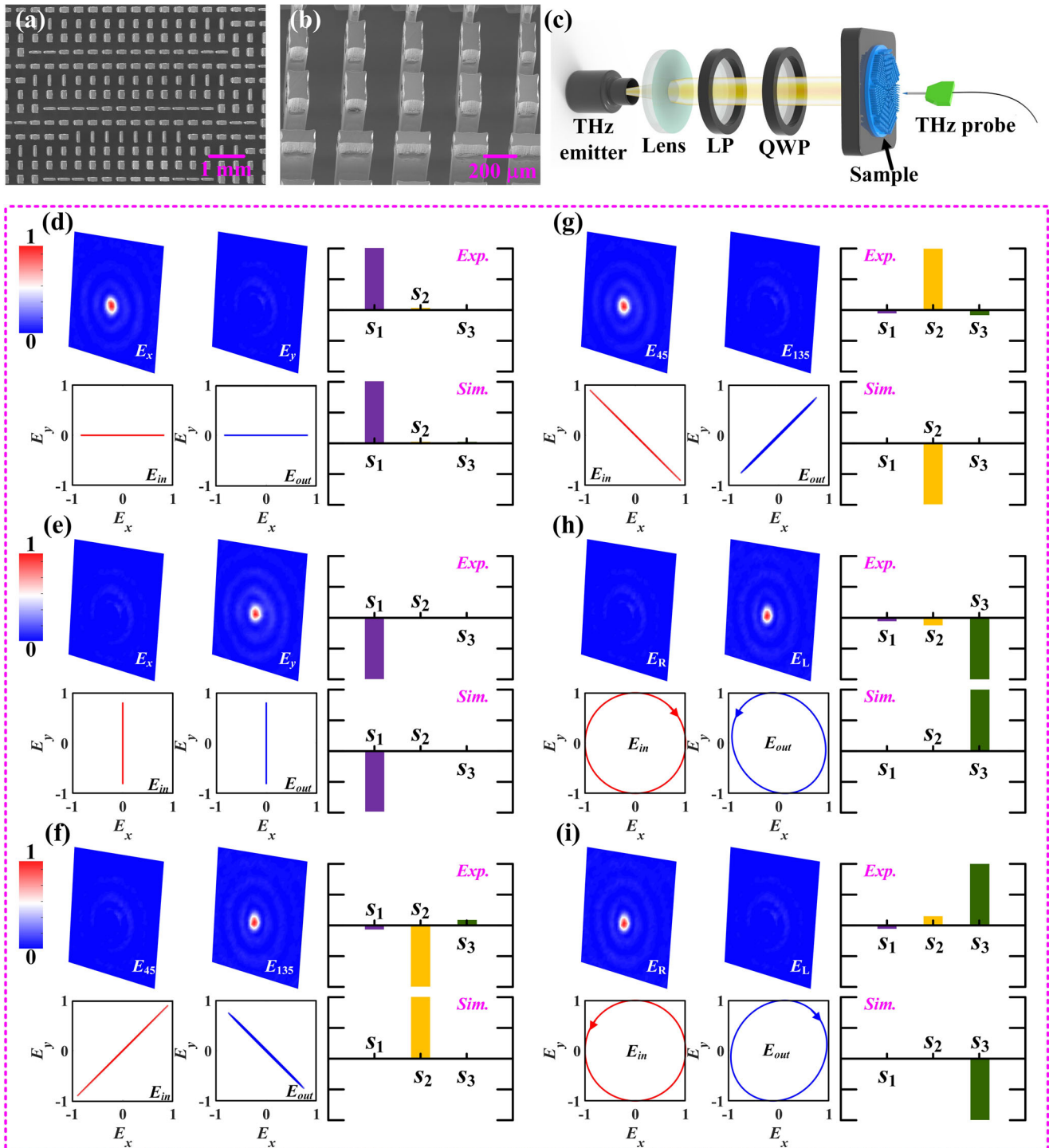


Figure 3. Experimental results of the fabricated metasurface samples with tightly focused properties. a,b) Samples obtained using inductively coupled plasma (ICP) etching technique, based on silicon wafers with a thickness of 1 mm. c) Schematic of basic experimental setup. LP: linear polarizer. QWP: quarter-wave plate. The normalized experimental results were used to reconstruct the full-Stokes parameter matrix as well as the profiles of the polarization ellipse under d) x-linearly polarized, e) y-linearly polarized, f) 45°-linearly polarized, g) 135°-linearly polarized, h) RCP, and i) LCP illuminations.

the transmission mode when illuminated by the residual polarization states. As recorded in the polarization ellipse plotted in Figure 3f, when we switch the incident polarization to 45° linear polarization, the transmitted field carries a polarization mode exactly orthogonal to the incident polarization, i.e., 135° linear polarization. This behavior is also clearly reflected in the reconstructed full-Stokes parameter matrix by monitoring the complex amplitude at the central pixel point of the E_{135} -component. Consequently, the same phenomenon is also recorded on the focal plane after illumination by three types of incident polarization that have not yet been introduced, as shown in Figure 3g–i. It is worth noting that, except for the polarization component of the electric field with orthogonal properties as shown in Figure 3, the S -parameters calculated from the normalized intensity of the residual transmitted polarization components to characterize the full-Stokes parameter matrix are equal to zero, as shown in Figure S4 (Supporting Information Note S4).

To further highlight the capability of the proposed design to reconstruct the full-Stokes parameter matrix for arbitrary incidence, we plot the electric field for each component in the focal plane for the incidence of randomly generated orthogonal polarization pairs in Figure S5 (Supporting Information Note S5). Obviously, the variability of the focusing intensity of the individual polarization components profoundly illustrates the orthogonality between the incident and transmitted polarization modes. This design can easily manage either arbitrary linear or elliptical polarization incidence, including the reconstructed parameter matrix as well as the polarization ellipse. In other words, the proposed multiplexed meta-platforms with a single focused spot can effectively simplify the complexity of arbitrary polarization in readout. In fact, the division of the focal plane allows to obtain different polarization information within a single snapshot, i.e., the information carried in relation to polarization is assigned to different polarization states or spectral components. Not only that, encrypted meta-holograms constructed from binary dot arrays can be realized by the proposed mechanism. Specifically, using the nonreciprocal property of the S -parameters in the matrix, i.e., S_1 is determined jointly by E_x and E_y , S_2 by E_{45} and E_{135} , and S_3 by E_R and E_L . As shown in Figure S6 (Supporting Information Note S6), 25 binary focal spots can exist simultaneously in the focal plane when x -polarized waves illuminate such meta-lens vertically. It is worth mentioning that the conversion from the incident x -polarization to an arbitrary polarization state dominates in the design profile containing binary information. The crossover arrangement of 0s and 1s prompts the feasibility of presenting complementary images within two orthogonal polarization channels and carrying correspondingly homogenous polarization states at the focal spots. In other words, by combining binary coding with polarization measurement, the desired transmitted information can be hidden in different polarization components. Although a binary image containing a 5×5 array of dots is simple, it can be used to store encrypted information.

To further emphasize the resolvability of the multiplexed metasurface with the single focusing capability for arbitrary polarized illumination, we proceed to reconstruct the transmitted polarization behavior using the E_z -component at the focal plane. It is well known that vortex beams with tightly focused properties can attract the conversion of spin angular momentum (SAM) to orbital angular momentum (OAM) of photons in the longitudinal

direction.^[45–48] This means that the SAM of the CP component contained in the incident beam can be partially transferred to the OAM of the longitudinally polarized electric field, producing a longitudinally polarized beam. The electric field distribution (E_z) of the longitudinally polarized component of the resulting tightly focused beam exhibits a typical doughnut-shaped profile with a topological charge of 1 or -1 . Thus, the distribution of the electric field in the focal plane of the E_z -component produced by the metasurface under linearly polarized illumination is a coherent superposition of two tiny vortex spots with topological charges of -1 and -1 . The detailed parametric derivation model can be found in the Supporting Information Note S7. The focusing behavior with an elongated focal depth can effectively attenuate the errors introduced in the measurements, so that the phase profiles embedded within the LCP and RCP channels can be described as^[31]

$$\begin{cases} \varphi_L(x, y) = \frac{k_0(x^2 + y^2)}{2[f_L + \Delta f_L \cdot (x^2 + y^2)/R^2]} \\ \varphi_R(x, y) = \frac{k_0(x^2 + y^2)}{2[f_R + \Delta f_R \cdot (x^2 + y^2)/R^2]} \end{cases} \quad (11)$$

where k_0 denotes the wave vector in free-space, $f_L = f_R = 5$ mm represents the initial focal depth, $\Delta f_L = \Delta f_R = 1$ mm indicates the extended focal length, R is radius of the meta-lenses. Thanks to the E_z -component generated in the propagation path by a tightly focused beam with extended depth, the imparted polarization characteristics can distinguish different incident modes. To the best of our knowledge, the axial electric field (E_z -component) generated by such beam in the longitudinal direction has many novel properties.^[48] The detection of incident polarization states by employing the spot shape of the far-field E_z -component in combination with optical image processing has not been reported in the THz band. The working mechanism for reconstructing an arbitrary linear polarization state using the E_z -component generated in the far-field mode is shown in Figure 4a.

Initially, we evaluated the electric field profiles of the E_z -component in the target plane under linearly polarized illumination using the designed metasurface. The simulation results obtained by the commercial software CST MICROWAVE STUDIO, and the incident linear polarization state can be described as γ -polarization. As γ gradually increases from 0° to 135°, it is as if a certain point located on the Poincaré sphere is rotating counterclockwise along its equator, as shown in Figure 4b. The fabricated samples were evaluated by fixing the transmittance axis of the analyzer at an angle of 0° (red arrows) with respect to the x -direction. Conventional linearly γ -polarized waves in the propagation direction can be generated by rotating the LP and QWP elements with respect to the x -axis, as displayed in Figure 3c. Unfortunately, the E_{zx} and E_{zy} components can only be obtained by rotating the sample using a THz near-field detecting system equipped with a probe (TeraSpike TD-800-Z). Subsequently, the desired polarization components are obtained using the superposition of the complex amplitude information recorded in the focal plane, i.e., $E_{z\gamma} = (E_{zx} \pm E_{zy})/\sqrt{2}$, and $E_{z\sigma} = (E_{zx} - i\sigma E_{zy})/\sqrt{2}$.^[41] Here, $E_{z\gamma}$ denotes the complex amplitude obtained under linearly polarized incidence while $E_{z\sigma}$ denotes

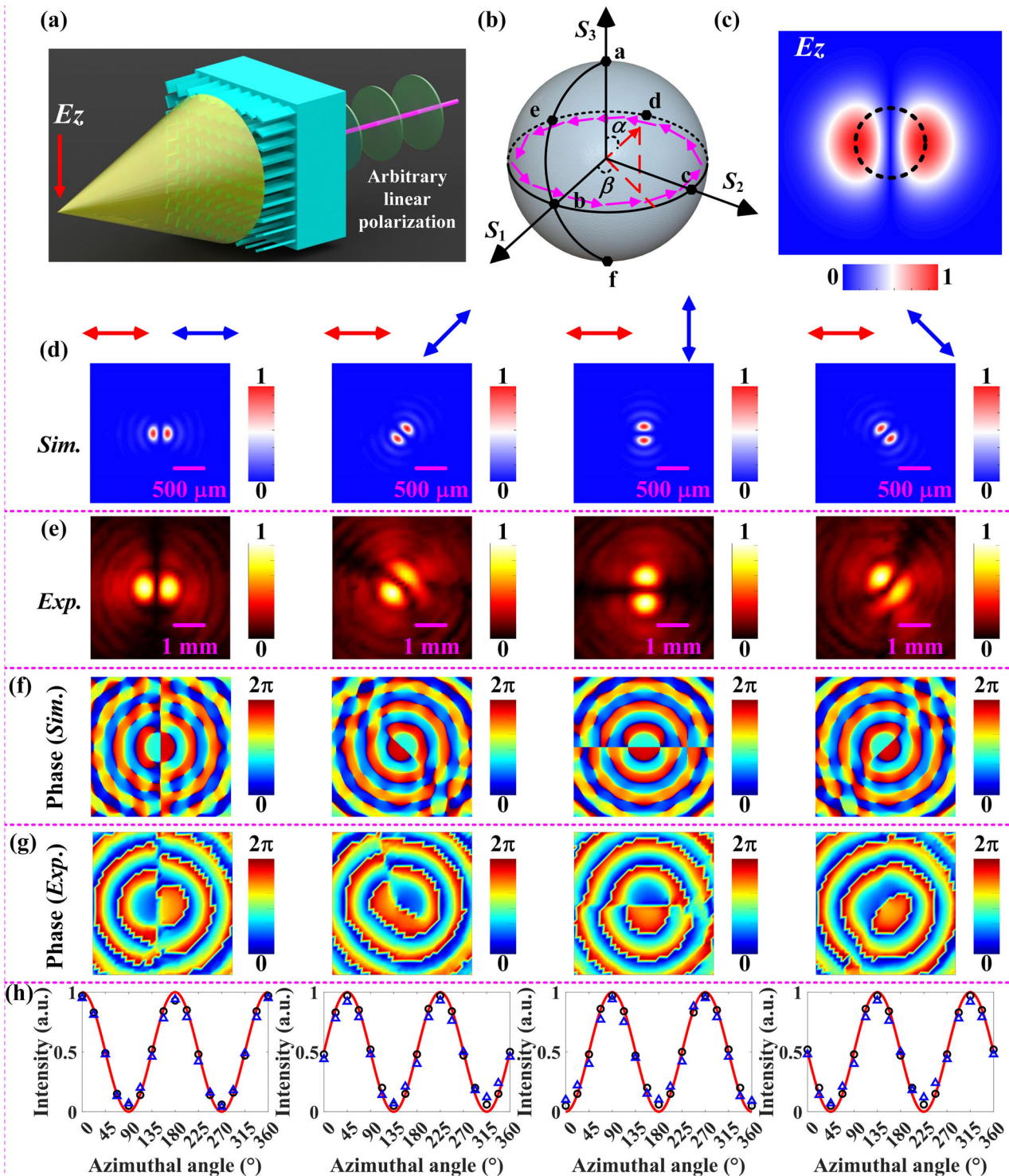


Figure 4. Experimental results obtained using a THz near-field scanning system equipped with a z-microprobe. a) Schematic diagram of the detection behavior of the incident linear polarization state utilizing the E_z -component generated in the focal plane. b) Introduced for representing the evolutionary trend of the incident linear polarization state of the Poincaré sphere. c) Schematic diagram for collecting the normalized amplitude distribution of the longitudinal electric field components generated in the focal plane. d) Simulated normalized distributions on the focal plane for $\gamma = 0^\circ, 45^\circ, 90^\circ,$ and 135° . e) Experimental normalized distributions on the focal plane for $\gamma = 0^\circ, 45^\circ, 90^\circ,$ and 135° . f) Simulated phase profiles on the focal plane for $\gamma = 0^\circ, 45^\circ, 90^\circ,$ and 135° , respectively. g) Measured phase distributions on the focal plane for $\gamma = 0^\circ, 45^\circ, 90^\circ,$ and 135° , respectively. h) Normalized curves extracted from the amplitude distributions along the black dashed path in (c) for $\gamma = 0^\circ, 45^\circ, 90^\circ,$ and 135° , where the solid red line represents the theoretical value, and the black circle and blue triangle indicate the simulation results and experimental results, respectively. The red (blue) arrows represent the transmitted (incident) polarization direction.

the complex amplitude recorded in the focal plane under CP incidence, and $\sigma = +1$ and $\sigma = -1$ represent the transmitted LCP and RCP components, respectively. The blue arrows represent the incident polarization state in all electric field distribution images. As shown in Figure 4d, the polarization angle of the incident THz wave can be clearly distinguished from the distribution of the beams produced on the focal plane. In other words, the brightest component contained in the petal-shaped profile is along the γ -direction when $\gamma = 0^\circ, 45^\circ, 90^\circ$, and 135° . Considering that the transmitted electric field distribution originates from the coherent superposition of the LCP and RCP components, i.e., $\vec{E} = [1 + \cos^2(l\psi + \gamma + \chi)]/2$.^[49,50] Here, ψ represents the major angle of the petals contained in the E_z -component under linearly polarized illumination, χ corresponds to transmitted polarization direction, and $l = \pm 1$ denotes the topological charges carried in the LCP and RCP channels. When \vec{E} takes the maximum value, then the parameter $\psi_{\max} = (n\pi - \gamma - \chi)/|l|$, ($n = 0, 1, \dots, |2l-1$). It means that the major angle of the vortex petal with $|2l|$ symmetry generated at the focal plane with respect to the horizontal direction can be simplified to $\psi_{\max} = -\gamma$. Therefore, the electric field distribution map after *mirroring* can clearly distinguish the polarization direction of the incident mode.

The experimental results are in high agreement with the results obtained from the simulation, as shown in Figure 4e. The phase maps recorded during the simulation and experiment are plotted in Figure 4f,g, respectively. Also, the phase profile carried by the monitored E_z -component has a typical discontinuity, i.e., the phases corresponding to the individual petal distributions are different. In addition, we calculate more meticulously the correspondence between the parameter γ possessed by the incident linear polarization and the lobe direction of the E_z -component using the time-domain finite integration method, as mentioned in the Supporting Information Note S8. To further illustrate the superiority of the longitudinal polarization component for polarization measurement, the amplitude distribution was extracted along the azimuthal direction of the resulting interference pattern at the focal plane, as shown by the black looped path in Figure 4c. The pixelated focal plane allows us to find the pixel point where the maximum value is located and can be used as a candidate to plot the azimuthal amplitude distributions at $\gamma = 0^\circ, 45^\circ, 90^\circ$, and 135° , respectively, as shown in Figure 4h. The solid red line in the image represents the theoretical value while the black circles and blue triangles indicate the amplitude distributions extracted from the simulated and experimental results, respectively. It can be clearly seen that the maximum values of the normalized amplitude distribution correspond to $0^\circ, 45^\circ, 90^\circ$, and 135° as the incident polarization angle gradually increases. Fortunately, the maximum absolute error corresponding to the results measured in the experiment is 7.4° , and the average absolute error is below 3.1° , which meets the expected design requirements. Although the employment of pixelated microprobes limits the application of the proposed design principle in some scenarios, the interpolation algorithm as well as the application of high aspect ratio (AR) silicon columns greatly improves the spatial resolution of the focused images compared to the report in ref. [51]. The EM response of a high AR dielectric column with periodic boundary conditions is described in the Supporting Information Note S9 under x - and y -polarized illumination, respectively. Thus, the linear polarization direction of the input THz

waves can be distinguished by the distribution of the interference pattern on the focal plane.

To characterize the ability of the longitudinal polarization component produced by the metasurface device to reconstruct the vector ellipse, the interference pattern generated in the focal plane under randomly incident polarization illumination with different ellipticity is shown in Figure 5. The pair of orthogonal polarization channels used to record the evolutionary trend of parameter S_3 was employed, as shown in Figure 5a₁. Not surprisingly, the electric field generated by the metasurface under LCP illumination shows a typical doughnut-shaped distribution. On the other hand, the RCP-based illumination similarly evokes a doughnut-shaped electric field profile at the focal plane, as displayed in Figure 5a₂. From Figure 5b_{1,2}, it can be observed that the experimentally measured results are in agreement with the simulated. In addition, unlike the phase distribution on the focal plane under linearly polarized illumination, the phase profile obtained at CP incidence has good continuity behavior, and the topological charge carried by the interference pattern can be clearly distinguished, as shown in Figure 5c_{1,2}. Benefiting from the photon conversion effect from SAM to OAM, we can conveniently extrapolate the topological charge carried by the beam under LCP and RCP illumination to be -1 and 1 , respectively, as shown in Figure 5d_{1,2}. In other words, by monitoring the electric field distributions and phase profiles of E_z -component under polarized THz wave illumination, we can quickly reconstruct the full-Stokes parameter matrix of the incident polarization state. The electric field distribution on the focal plane was pixelated using an approach similar to that in Figure 4c, and the normalized amplitude distribution was obtained as shown in Figure 5e_{1,2}. Clearly, the results shown in the images further illustrate the effectiveness of the proposed metasurface analyzer.

So far, we have successfully reconstructed the full-Stokes parameter matrix using the longitudinal polarization component produced by such tightly focused beam. Subsequently, the generated random polarization states were used to illuminate this multiplexed metasurface, and the processed simulation and experimental results are shown in Figure 5a_{3,4}, b_{3,4}, respectively. It is well known that the polarization ellipse is a visual approach used to characterize polarized THz waves, whose properties can be described by three key parameters, such as handedness, azimuthal angle, and ellipticity. It is not difficult to find that the continuity of the phase distribution imparts the resolvability of the randomly incident polarization state, i.e., the chirality of the polarization ellipse. Correspondingly, the simulated and experimental results recorded in the focal plane are shown in Figure 5c_{3,4}, d_{3,4}, respectively. As can be seen from the blue outline at the top of Figure 5, the orientation angles of the selected elliptical polarization with respect to the horizontal direction are 90° and 0° , respectively. It is interesting to note that the maximum value of the normalized amplitude curve corresponds exactly to the azimuthal angle of the polarization ellipse, as displayed in Figure 5e_{3,4}. Based on the experimental results obtained in Figure 5b_{1,2}, the electric field distribution at the incidence of the elliptical polarization state was reconstructed using the polarization decomposition method, as shown in Figure 5b_{3,4}. Obviously, there is good agreement between the experimental and simulation results, and the little deviation may attribute to the nonuniformity of the incident waves.

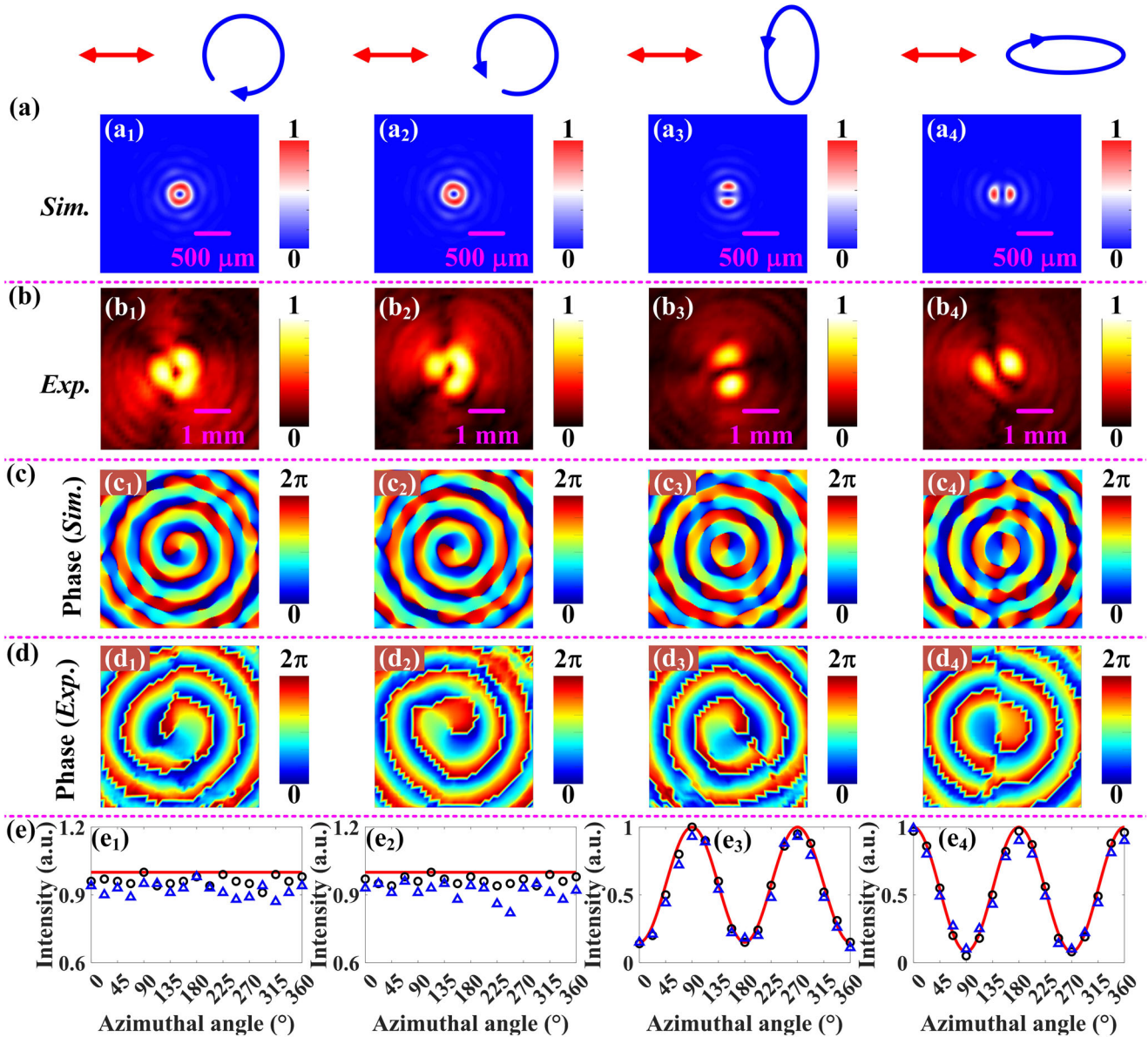


Figure 5. The electric field distribution of the designed metasurface under circular or elliptical polarization incidence obtained by the method of polarization transformation. a_1 – a_4) Simulated normalized electric field distributions on the focal plane at the incidence of RCP, LCP, left-handed elliptically polarized (LEP), and right-handed elliptically polarized (REP). b_1 – b_4) Experimental normalized electric field distributions on the focal plane at the incidence of RCP, LCP, LEP, and REP. c_1 – c_4) Simulated phase distributions on the focal plane at the incidence of RCP, LCP, LEP, and REP. d_1 – d_4) Measured phase profiles on the focal plane at the incidence of RCP, LCP, LEP, and REP. e_1 – e_4) Normalized curves extracted from the amplitude distributions along the black dashed path in Figure 4c at the incidence of RCP, LCP, LEP, and REP, respectively. The red (blue) arrows represent the transmitted (incident) polarization direction.

Then, we define a movable point on the Poincaré sphere to further illustrate the superiority of the longitudinal polarization component for polarization measurement, as displayed in Figure 6b. The electric field and phase profiles generated at the predefined focal plane were monitored using the polarization state represented by the defined point during its movement along the path $b \rightarrow a \rightarrow d$ as the incident mode, as shown in Figure 6a. In fact, the parameter α describes the evolutionary trend of the incident polarization state during the movement of the defined

point along the path $b \rightarrow a \rightarrow d$. Therefore, establishing a theoretical model between the parameter α and the ellipticity η is the key event. As illustrated in the inset in Figure 6c, the normalized intensities represented at points A, B, C, and D can be defined as I_A , I_B , I_C , and I_D , respectively, in the closed-loop path. Herein, I_A and I_B represent the two maximum intensity spots while I_C and I_D represent the two minimum intensity spots in the distributions. In order to weaken the real errors in the measurement process, the ellipticity η of the incident polarization can be

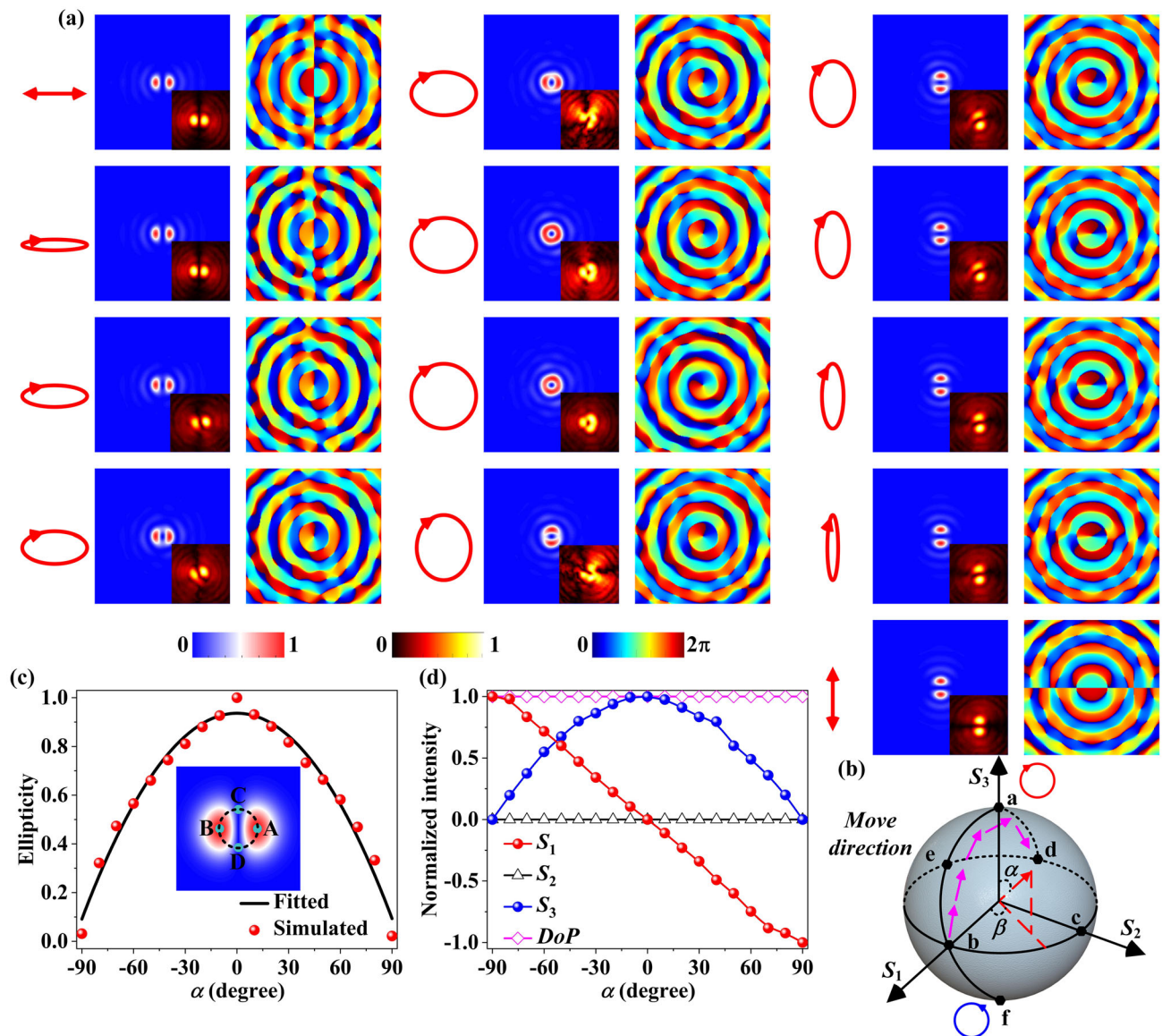


Figure 6. Using the parametric theoretical model developed by E_z -component in the measurement of randomly incident polarization states. a) The normalized electric field distribution in the focal plane monitored as the polarization state carried by the incident THz wave moves along the path $b \rightarrow a \rightarrow d$ on the Poincaré sphere. b) Schematic diagram of the evolution of the polarization state along path $b \rightarrow a \rightarrow d$ located on the Poincaré sphere. c) The normalized amplitude distribution extracted along the closed loop path $A \rightarrow C \rightarrow B \rightarrow D$ in the pixelated focal plane as a function of the ellipticity of the incident polarization state. d) The trends of the reconstructed full-Stokes parameters as well as the DoP during the evolution of the incident polarization state along path $b \rightarrow a \rightarrow d$, where α is located in the interior of the Poincaré sphere and is used to characterize the evolution of the polarization states. The red arrows represent the incident polarization direction.

calculated by the intensity ratio corresponding to each spot, which can be described as^[52]

$$\eta = \sqrt{(I_C + I_D)/2} / \sqrt{(I_A + I_B)/2} \quad (12)$$

Obviously, $\eta = 1$ and $\eta = 0$ correspond to circularly and linearly polarized incidence. The pixelated focal plane allows us to extract the normalized amplitude intensity on the path $A \rightarrow C \rightarrow B \rightarrow D$ by coded methods. Thus, for an arbitrary elliptical polarization in-

cidence, the key parameter η can still be obtained using the E_z -component.

The incident polarization state represented by the point located on the Poincaré sphere gradually converts from horizontal polarization to RCP as it moves from b to a along the predefined path, as shown by the red marker in Figure 6a. It can be clearly seen that the evolution of the interference pattern produced on the focal plane shows a gradual trend from petal to doughnut shape, with the parameter α gradually increasing from -90° to 0° . Also, with the parameter α gradually increasing from 0° to 90° , the resulting electric field profile gradually changes from doughnut to

petal shapes. More elaborate predictions can be made by developing generalized parametric theoretical models to characterize the relationship between the parameter α as a function of the extracted ellipticity, as shown in Figure 6c. By extending the 13 incidence methods as shown in Figure 6a, a more sophisticated data acquisition guarantees the effectiveness of the prediction model. It is interesting to note that the function obtained by fitting the parameter α to the ellipticity η exhibits typical parabolic properties. The coefficients used to characterize the second-order, first-order, and constant terms in the function are calculated as $-1.042\text{e-}04$, $1.251\text{e-}05$, and 0.9363 , respectively. In addition, we calculate the trend of the S -parameters that comprise the full Stokes matrix as the parameter α , used to represent the incident polarization state, gradually increases from -90° to 90° . Since the predefined path coincides with the meridian on the Poincaré sphere, the parameter S_1 will undergo a variation from -1 to 1 . The employment of the control variables method guarantees the plausibility of the prediction model, so that the handedness of the incident polarization state remains unchanged. Thus, the curve in Figure 6d concerning parameter S_3 reasonably shows the evolutionary trend of the handedness. Furthermore, the phase profile monitored at the focal plane illustrates the same evolutionary trend described above, as shown in Figure 6a. However, the parameter S_2 always remains constant because the starting point b (horizontal polarization) and the ending point d (vertical polarization) of the defined path are located on the straight line representing the parameter S_1 . In addition, we calculated the DoP (degree of polarization, expressed as $\text{DoP} = \sqrt{S_1^2 + S_2^2 + S_3^2/S_0^2}$) of the transmitted polarization for illustrating the completely polarized characteristics of the transmitted THz waves. Benefiting from the demonstrated meta-device that can work in single excitation, it can be applied to characterize the incident polarization state by a single snapshot with high accuracy.

4. Conclusions

In conclusion, we propose and demonstrate a novel method for measuring the polarization state of incident THz waves using all-silicon metasurfaces generated based on polarization multiplexing techniques. The full-Stokes parameter matrix associated with the incident polarization state can be effectively reconstructed by extracting the complex amplitudes at the focal plane of multiplexed meta-platforms with a single focal spot. Moreover, the employment of the polarization elliptic equation more precisely evaluates the polarization detection capability of the proposed mechanism in the THz band. Benefiting from the resolvability of the pixelated focal plane, we evaluate the incident polarization state by applying the longitudinal polarization component E_z carried by the resulting beam with tightly focused characteristics. Moreover, by monitoring the normalized intensity distribution and phase profile of the E_z -component at the focal plane, the two key parameters that determine the trajectory of the incident electric field, i.e., azimuthal angle and handedness, are ingeniously reconstructed. Ultimately, the parametric theoretical model is developed to completely predict the evolution of the incident polarization state and determine the ellipticity of the polarization ellipse. Therefore, such efficient meta-platforms provide a promising method for evaluating the SoP of THz waves, accelerates the

practical application of THz radiation in high-resolution imaging, sensing, and so on.

5. Experimental Section

Sample Fabrication: The selected basic material for all-dielectric metasurfaces operating in the 0.5–2 THz range was generally silicon with a dielectric constant $\epsilon = 11.9$. A standard high-resistance silicon wafer with a thickness of 1 mm and a radius of 2 in. was used as a candidate, whose transmission coefficient at the target frequency (0.8 THz) was about 0.9 affected by the Fabry–Perot resonance. First, the wafer needed to be cleaned to remove various contaminants from its surface. Then, a photoresist film with a thickness of about 6.8 μm could be obtained by spin-coating the positive photoresist AZ 4620. The obtained mask was aligned with the silicon wafer and exposed, and the desired pattern could be obtained after development. Subsequently, the obtained array was etched by introducing the ICP etching technique (STS MULTIPLEX ASE-HRM ICP ETCHER, UK) with a depth of 400 μm . Last, the fabricated arrays were washed using acetone and separated to obtain the sample to be measured.

Experimental Steps: To obtain the pixelated focal plane in transmission mode, a terahertz near-field imaging system (TeraCube Scientific M2) was employed to measure the fabricated samples, as shown in Figure 3c. The femtosecond laser source used in the system was 780 nm with 100 fs pulse width and 80 MHz repetition rate. The sample was scanned using a polarization system equipped with a microprobe and the electric field distribution on the focal plane was recorded pixel-by-pixel. In the experiment, a linearly polarized terahertz beam was generated from a commercially available photoconductive antenna and collimated by a TPX terahertz lens. The incident terahertz wave was then illuminated vertically from the substrate side of the fabricated all-silicon sample in order to produce a target spot on a pre-designed focal plane. Then, the generated electric field components were detected by a commercial terahertz near-field probe, which was placed ≈ 5.2 mm above the sample during the measurement. Subsequently, the different polarization components were recorded by rotating the sample and changing the microprobes. Finally, polarization calculations were performed using standard code to yield the desired electric field distribution.

Supporting Information

Supporting Information is available from the Wiley Online Library or from the author.

Acknowledgements

This work was supported by the National Key Research and Development Program of China (no. 2021YFB2800703), National Natural Science Foundation of China (nos. U22A2008, 62075159, 62275190), Laboratory Foundation (no. 2022JQJLB055006), and Laoshan Laboratory Science and Technology Innovation Project (no. LSKJ202200801).

Conflict of Interest

The authors declare no conflict of interest.

Data Availability Statement

The data that support the findings of this study are available from the corresponding author upon reasonable request.

Keywords

all-silicon multiplexed metasurfaces, full-stokes parameters, longitudinal polarization component, tightly focusing behavior

Received: May 12, 2023

Revised: June 27, 2023

Published online:

- [1] N. A. Rubin, G. D'Aversa, P. Chevalier, Z. Shi, W. Chen, F. Capasso, *Science* **2019**, 365, eaax1839.
- [2] Y. Han, G. Li, *Opt. Express* **2005**, 13, 7527.
- [3] S. B. Powell, R. Garnett, J. Marshall, C. Rizk, V. Gruev, *Sci. Adv.* **2018**, 4, eaao6841.
- [4] S. Wei, Z. Yang, M. Zhao, *Opt. Lett.* **2017**, 42, 1580.
- [5] M. Dai, C. Wang, B. Qiang, F. Wang, M. Ye, S. Han, Y. Luo, Q. Wang, *Nat. Commun.* **2022**, 13, 4560.
- [6] B. Schaefer, E. Collett, R. Smyth, D. Barrett, B. Fraher, *Am. J. Phys.* **2007**, 75, 163.
- [7] E. Compain, B. Drevillon, *Appl. Opt.* **1998**, 37, 5938.
- [8] H. Xu, G. Hu, Y. Wang, C. Wang, M. Wang, S. Wang, Y. Huang, P. Genevet, W. Huang, *Light: Sci. Appl.* **2021**, 10, 75.
- [9] H. Cai, J. A. Dolan, G. S. D. Gordon, T. Chung, D. López, *ACS Photonics* **2021**, 8, 2581.
- [10] I. Javed, J. Kim, M. A. Naveed, D. K. Oh, D. Jeon, I. Kim, M. Zubair, Y. Massoud, M. Q. Mehmood, J. Rho, *ACS Appl. Mater. Interfaces* **2022**, 14, 36019.
- [11] D. Goldstein, *Polarized Light*, 2nd ed., Marcel Dekker, New York **2003**.
- [12] H. G. Berry, G. Gabrielse, A. E. Livingston, *Appl. Opt.* **1977**, 16, 3200.
- [13] R. Shogenji, Y. Kitamura, K. Yamada, S. Miyatake, J. Tanida, *Opt. Express* **2004**, 12, 1643.
- [14] R. C. Devlin, A. Ambrosio, N. A. Rubin, J. P. B. Mueller, F. Capasso, *Science* **2017**, 358, 896.
- [15] M. Khorasaninejad, K. B. Crozier, *Nat. Commun.* **2014**, 5, 5386.
- [16] A. Shaltout, J. Liu, A. Kildishev, V. Shalaev, *Optica* **2015**, 2, 860.
- [17] J. Wei, Y. Chen, Y. Li, W. Li, J. Xie, C. Lee, K. S. Novoselov, C. Qiu, *Nat. Photonics* **2023**, 17, 171.
- [18] J. Pros, M. G. Nielsen, S. I. Bozhevolnyi, *Optica* **2015**, 2, 716.
- [19] F. Ding, A. Pors, Y. Chen, V. A. Zenin, S. I. Bozhevolnyi, *ACS Photonics* **2017**, 4, 943.
- [20] E. Arbabi, S. M. Kamali, A. Arbabi, A. Faraon, *ACS Photonics* **2018**, 5, 3132.
- [21] Y. Ren, S. Guo, W. Zhu, P. Huo, S. Liu, S. Zhang, P. Chen, L. Chen, H. J. Lezec, A. Agrawal, Y. Lu, T. Xu, *Adv. Photonics Res.* **2022**, 3, 2100373.
- [22] M. Khorasaninejad, W. Chen, A. Zhu, J. Oh, R. Devlin, D. Rousso, F. Capasso, *Nano Lett.* **2016**, 16, 4595.
- [23] P. C. Wu, J.-W. Chen, C.-W. Yin, Y.-C. Lai, T. L. Chung, C. Y. Liao, B. H. Chen, K.-W. Lee, C.-J. Chuang, C.-M. Wang, *ACS Photonics* **2017**, 5, 2568.
- [24] Z. Yang, Z. Wang, Y. Wang, X. Feng, M. Zhao, Z. Wan, L. Zhu, J. Liu, Y. Huang, J. Xia, *Nat. Commun.* **2018**, 9, 4607.
- [25] T. Sun, J. Hu, X. Zhu, F. Xu, C. Wang, *Laser Photonics Rev.* **2022**, 16, 2100650.
- [26] R. Wang, J. Han, J. Liu, H. Tian, W. Sun, L. Li, X. Chen, *Opt. Lett.* **2020**, 45, 3506.
- [27] Z. Jiang, J. Lu, J. Fan, J. Liang, M. Zhang, H. Su, L. Zhang, H. Liang, *Laser Photonics Rev.* **2023**, 17, 2200484.
- [28] J. P. B. Mueller, N. A. Rubin, R. C. Devlin, B. Groever, F. Capasso, *Phys. Rev. Lett.* **2017**, 118, 113901.
- [29] H. Xu, L. Han, Y. Li, Y. Sun, J. Zhao, S. Zhang, C. Qiu, *ACS Photonics* **2019**, 6, 211.
- [30] Y. Yuan, S. Sun, Y. Chen, K. Zhang, X. Ding, B. Ratni, Q. Wu, S. Burokur, C. Qiu, *Adv. Sci.* **2020**, 7, 2001437.
- [31] H. Li, S. Duan, C. Zheng, J. Li, H. Xu, C. Song, J. Li, F. Yang, W. Shi, Y. Zhang, Y. Shen, J. Yao, *Adv. Opt. Mater.* **2023**, 11, 2202461.
- [32] Z. Wang, Y. Yao, W. Pan, H. Zhou, Y. Chen, J. Lin, J. Hao, S. Xiao, Q. He, S. Sun, L. Zhou, *Adv. Sci.* **2023**, 10, 2205499.
- [33] S. Dong, S. Li, X. Ling, G. Hu, Y. Li, H. Zhu, L. Zhou, S. Sun, *Appl. Phys. Lett.* **2022**, 120, 181702.
- [34] H. Li, C. Zheng, H. Xu, J. Li, C. Song, J. Li, L. Wu, F. Yang, Y. Zhang, W. Shi, J. Yao, *Nanoscale* **2022**, 14, 12856.
- [35] E. Collett, B. Schaefer, *Appl. Opt.* **2008**, 47, 4009.
- [36] J. Wei, C. Xu, B. Dong, C. Qiu, C. Lee, *Nat. Photonics* **2021**, 15, 614.
- [37] G. Wang, T. Zhou, J. Huang, X. Wang, B. Hu, Y. Zhang, *Photonics Res.* **2023**, 11, 100.
- [38] X. Cai, R. Tang, H. Zhou, Q. Li, S. Ma, D. Wang, T. Liu, X. Ling, W. Tan, Q. He, S. Xiao, L. Zhou, *Adv. Photonics* **2021**, 3, 036003.
- [39] C. Zheng, J. Li, J. Liu, J. Li, Z. Yue, H. Li, F. Yang, Y. Zhang, Y. Zhang, J. Yao, *Laser Photonics Rev.* **2022**, 16, 2200236.
- [40] Y. Lang, Q. Xu, X. Chen, J. Han, X. Jiang, Y. Xu, M. Kang, X. Zhang, A. Alù, J. Han, W. Zhang, *Laser Photonics Rev.* **2022**, 16, 2200242.
- [41] J. Li, C. Zheng, J. Li, G. Wang, J. Liu, Z. Yue, X. Hao, Y. Yang, F. Li, T. Tang, Y. Zhang, Y. Zhang, J. Yao, *Photonics Res.* **2021**, 9, 10.
- [42] S. Xiao, T. Wang, T. Liu, C. Zhou, X. Jiang, J. Zhang, *J. Phys. D: Appl. Phys.* **2020**, 53, 503002.
- [43] S. Gao, C. Zhou, W. Yue, Y. Li, C. Zhang, H. Kao, C. Li, S. Lee, D. Choi, *ACS Appl. Mater. Interfaces* **2021**, 13, 12.
- [44] X. Li, H. Wang, X. Xu, L. Ju, Z. Fan, S. Chen, *Opt. Commun.* **2021**, 484, 126690.
- [45] K. S. Youngworth, T. G. Brown, *Opt. Express* **2000**, 7, 77.
- [46] R. Dorn, S. Quabis, G. Leuchs, *Phys. Rev. Lett.* **2003**, 91, 233901.
- [47] C. Zheng, J. Li, J. Li, Z. Yue, H. Zhao, X. Hao, Y. Zhang, J. Yao, *Ann. Phys.* **2021**, 533, 2100159.
- [48] M. Gu, *Advanced Optical Imaging Theory*, Springer, Heidelberg **2000**.
- [49] Z. Zhang, J. Han, D. Geng, Y. Wang, A. Ma, *IEEE Photonics J.* **2021**, 13, 6.
- [50] H. Zang, Z. Xi, Z. Zhang, Y. Lu, P. Wang, *Sci. Adv.* **2022**, 8, eadd1973.
- [51] Y. Xu, H. Zhang, Q. Li, X. Zhang, Q. Xu, W. Zhang, C. Hu, X. Zhang, J. Han, W. Zhang, *Nanophotonics* **2020**, 9, 3393.
- [52] A. Ma, Y. Intaravanne, J. Han, R. Wang, X. Chen, *Adv. Opt. Mater.* **2020**, 8, 2000484.